The Astrophysical Journal, 954:99 (10pp), 2023 September 1 https://doi.org/10.3847/1538-4357/ace690

Submillimeter Observations of Magnetic Fields in Massive Star-forming Region W75N

Lingzhen Zeng[1], Qizhou Zhang[1], Felipe O. Alves[2], Tao-Chung Ching[3,4], Josep M. Girart[5,6], and Junhao Liu[7]
[1] Center for Astrophysics | Harvard & Smithsonian, 60 Garden Street, Cambridge, MA 02138, USA; lingzhen.zeng@cfa.harvard.edu
[2] Center for Astrochemical Studies, Max-Planck-Institut für extraterrestrische Physik (MPE), Gie/βenbachstr. 1, D-85741 Garching, Germany
[3] Research Center for Intelligent Computing Platforms, Zhejiang Lab, Hangzhou 311100, People's Republic of China
[4] National Radio Astronomy Observatory, 1003 Lopezville Road, Socorro, NM 87801, USA
[5] Institut de Ciències de l'Espai (ICE), CSIC, Can Magrans s/n, E-08193 Cerdanyola del Vallès, Catalonia, Spain
[6] Institut d'Estudis Espacials de Catalunya (IEEC), E-08034 Barcelona, Catalonia, Spain
[7] East Asian Observatory, 660 N. A'ohōkū Place, University Park, Hilo, HI 96720, USA
Received 2022 November 4; revised 2023 July 10; accepted 2023 July 10; published 2023 August 25

Abstract

This paper presents the results of full polarization observations of the massive star-forming region W75N, conducted with ∼3″ spatial resolutions at 345 GHz using the Submillimeter Array. The magnetic field structures in the dense cores of the region are derived using the linearly polarized continuum emission. The overall magnetic field strength and orientation are found to agree with those from the previous observations. The plane-of-sky component of the magnetic field in the region was calculated to be $\sim 0.8 \pm 0.1$ mG using the angular dispersion function method. Further analyses involving the polarization-intensity gradient-local gravity method and $H^{13}CO^+$ (4–3) line data indicated that the cloud is undergoing global gravitational collapse and the magnetic field is shaped by gravity and outflows in the dense core regions.

Unified Astronomy Thesaurus concepts: Circumstellar matter (241); Interstellar medium (847); Magnetic fields (994); Star formation (1569)

1. Introduction

Stars are born in dense molecular cores when self-gravity exceeds the internal support and drives gravitational collapse and the formation of an embedded protostar. In addition to gravity, both turbulence and magnetic fields influence the dynamical evolution of the molecular gas and impact the outcome of star formation. Solenoidal turbulence suppresses star formation since it acts similar to the thermal pressure that counteracts gravity, thus hindering star formation. Compressive turbulence, on the other hand, compresses the gas and enhances its densities, thus promoting star formation (Federrath et al. 2010; Menon et al. 2020). Magnetic fields, well coupled with the molecular gas, tend to restrict the movement of material along the field lines, thus hindering star formation (Hennebelle & Chabrier 2009; Myers et al. 2014).

There have been considerable efforts devoted to accessing the role of magnetic fields in star-forming dense molecular cores. Thanks to the improvement in sensitivity, polarimetric observations in the millimeter and submillimeter wavelengths become increasingly accessible to probe the plane-of-the-sky component of magnetic fields through linearly polarized dust emission (Zhang et al. 2014). We refer readers to recent reviews on the development of observational efforts on magnetic fields in molecular clouds and star formation (Hull & Zhang 2019; Pattle & Fissel 2019; Liu et al. 2022b; Pattle et al. 2022).

Despite the considerable progress, there is a lack of understanding on how magnetic fields may affect star formation in a protocluster environment where multiple stars arise from collapse and fragmentation of molecular gas. We present Submillimeter Array (SMA) observations of W75N, a massive star-forming region that contains a number of H II regions and is located in the local spiral arm at a distance of approximately 1.3 kpc (Rygl et al. 2012). W75N is part of the Cygnus-X giant molecular cloud, which spans over 100 pc and includes the renowned DR21 region.

Early observations of the region indicated that W75N IRS 1, a cluster of young stellar objects, powered a massive molecular outflow. Very Large Array (VLA) observations at 4.9 GHz detected three ionized regions, W75N(A), W75N(B), and W75N(C), near the center of the outflow (Haschick et al. 1981). Later, VLA 8.4 GHz observations revealed that W75N(B) consisted of three compact regions, Ba, Bb, and Bc (Hunter et al. 1994). Using 1.3 cm continuum VLA observations, Torrelles et al. (1997) discovered VLA 1 (Ba), VLA 3 (Bb), and another compact source located between them (VLA 2). Carrasco-González et al. (2010) suggested that source Bc was a radio Herbig–Haro object (Eisloffel et al. 2000) powered by the VLA 3 radio jet. They also discovered the VLA 4 source, located south of the VLA 1–VLA 3 group. Kim et al. (2013) found that the outflow of VLA 2 was in a transition from a shell-like to a more elongated jet-like shape based on very long baseline interferometry (VLBI) observations of 22 GHz water masers. Further observations by Surcis et al. (2014) showed that the water maser distribution around VLA 1 was stable, while the shell-like structure in VLA 2 was expanding along the direction parallel to the thermal radio jet of VLA 1, which was later confirmed by Carrasco-González et al. (2015). Recently, using VLA-A data covering 4–48 GHz, Rodríguez-Kamenetzky et al. (2020) concluded that Bc and VLA 4 were obscured Herbig–Haro objects excited by the jet from VLA 3.

Observations in millimeter wavelengths have revealed the presence of nine dense cores (MM1 to MM9) in the W75N region. These were identified using continuum data obtained with BIMA and CARMA (Shepherd 2001; Watson et al. 2002; Shepherd et al. 2003, 2004). The MM1 core was further studied using SMA and resolved into two compact continuum sources, MM1a and MM1b (Minh et al. 2010). In addition, a dense core

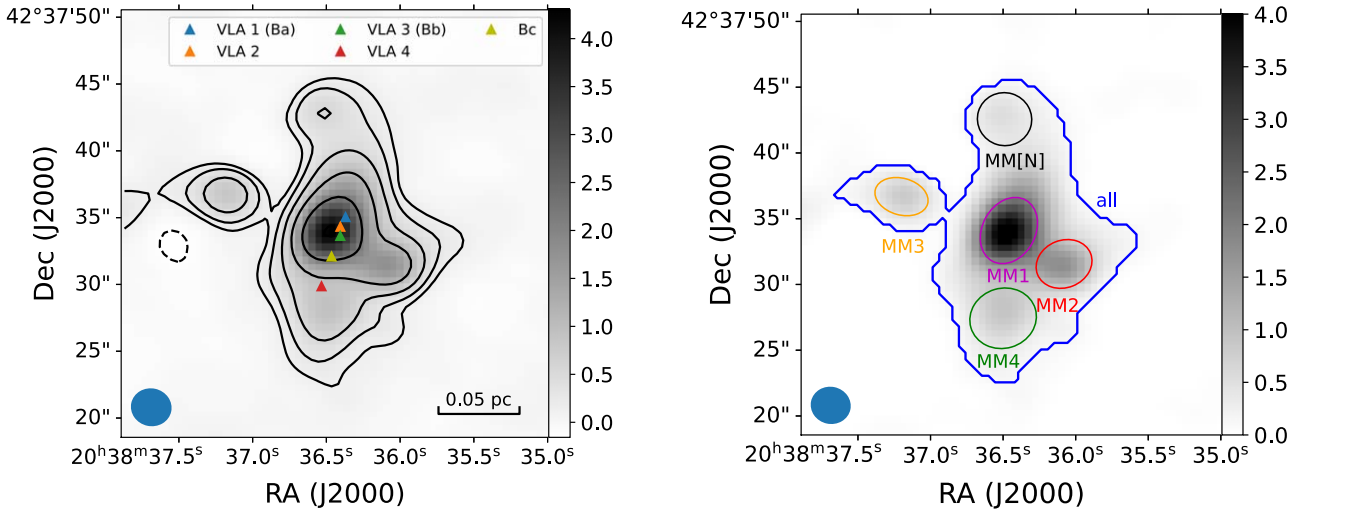

Figure 1. (a) 345 GHz continuum emission image of W75N. The synthesized beam marked in the lower left corner of the image is $3\farcs05 \times 2\farcs83$ at position angle (PA) $= 77\fdg8$. The intensity is shown in gray scales in units of Jy beam^{-1} with contour levels at [-5σ, 5σ, 10σ, 20σ, 40σ, 80σ, 160σ, and 320σ], where $\sigma =$ 26.1 mJy beam^{-1}. The previous detected compact sources are denoted by filled triangles. (b) Dense cores identified by CARTA are labeled as MM1, MM2, MM3, MM4, and MM[N]. The ellipses show the FWHMs from 2D Gaussian fits, while the blue color mask of the entire region is labeled as "all."

Table 1
Observational Summary

Observation Date	Number of Antennas	Array Configuration	Baseline Range (m)	Flux Calibrator	Gain Calibrator	Polarization and Bandpass Calibrator
2012 Jul 3	7	compact	16.5–32	Titan, Uranus	MWC349A	3c279
2012 Jul 4	7	compact	16.5–32	Titan	MWC349A	3c279
2012 Jul 5	7	compact	16.5–32	Titan, Uranus	MWC349A	3c84
2012 Aug 7	6	subcompact	9.5–25	Uranus	MWC349A	3c84
2012 Aug 8	6	subcompact	9.5–25	Uranus	MWC349A	3c84
2012 Aug 9	6	subcompact	9.5–25	Uranus	MWC349A	3c84

labeled as MM[N] was recently reported to the north of MM1 using Atacama Large Millimeter/submillimeter Array (ALMA) data at 1.3 mm (Rodríguez-Kamenetzky et al. 2020).

Previous polarization observations of W75N at 450, 870, and 1100 μm, using the James Clerk Maxwell Telescope (JCMT), yielded only a single polarization segment due to the large beam sizes of around 12″–19″ (Vallee & Bastien 1995; Greaves & Holland 1998). At 870 and 1100 μm, the inferred magnetic field had an average position angle of approximately 150°, while at 450 μm, it was measured to be around 37°. To improve the angular resolution, we conducted full polarization observations of the W75N region using the SMA with spatial resolutions of approximately 3″ at 345 GHz. In this study, we focus on the central region of W75N, which includes the MM1 to MM4, and MM[N] cores. We present the derived parameters of these dense cores using the dust continuum polarization data in this paper. We summarize the SMA observations in Section 2 and present the results in Section 3. A discussion of the results is shown in Section 4, followed by a summary in Section 5.

2. Observations and Data Reduction

The observations of W75N were carried out between 2012 July 3 and 2012 August 9 with the SMA (Ho et al. 2004). Three observations were made in July using the compact array configuration, and three were made in August using the subcompact configuration. The number of antennas in the array varied between six and seven. The observational parameters and calibration sources can be found in Table 1. The Application Specific Integrated Circuit (ASIC) correlator provided a 4 GHz intermediate frequency (IF) bandwidth (4–8 GHz) with a uniform spectral width of 812.5 kHz per channel. The receivers were tuned to the 345 GHz band, which captured the CO (3–2) and $H^{13}CO^+$ (4–3) lines, with a velocity resolution of approximately 0.70 km s^{-1}.

The visibility data from the observations were calibrated for bandpass, flux, and time-dependent gains using the IDL superset MIR package adapted for the SMA (Scoville et al. 1993). The calibrated data were then exported to the Miriad (Sault et al. 1995) format for instrumental polarization calibrations and imaging. Table 1 lists the calibrators used for each track. The synthesized beam size of the combined visibilities was approximately $3\farcs05 \times 2\farcs83$. The 1σ rms noise of the Stokes I image of the continuum emission was approximately 26.1 mJy beam^{-1}, while the rms noise of the Stokes Q/U maps after debiasing using the method from Vaillancourt (2006) was approximately 1.4 mJy beam^{-1}. The Astropy package (Astropy Collaboration et al. 2013, 2018) was used for the final analysis.

3. Results

3.1. Continuum Emission

Figure 1(a) illustrates the 345 GHz continuum emission of the W75N region. To identify dense structures in this area, we

Table 2
Observation Parameters of Dense Structures

Structure	R.A.(J2000) (hh:mm:ss)	Decl.(J2000) (dd:mm:ss)	Inegrated Flux (Jy)	FWHM $a'' \times b''$	Peak Intensity (Jy beam^{-1})	PA (deg)
all	20:38:36.44	42:37:33.75	17.9	9.2 × 7.4	2.3	19.6
MM1	20:38:36.46	42:37:34.11	10.2	5.2 × 4.1	4.1	146.9
MM2	20:38:36.08	42:37:31.54	3.0	4.5 × 3.5	1.7	106.1
MM3	20:38:37.20	42:37:36.69	1.1	4.1 × 2.8	0.9	75.2
MM4	20:38:36.50	42:37:27.57	2.3	5.2 × 4.6	0.8	98.7
MM[N]	20:38:36.49	42:37:42.57	1.1	4.1 × 4.0	0.5	73.2

applied the dendrogram algorithm (Rosolowsky et al. 2008) to the continuum data using the astrodendro[8] package. For the astrodendro analysis, we set the minimum value for the structure to be considered as 3σ, the minimum height required for an independent structure to be retained as 1σ, and the minimum number of pixels for a structure to be considered as half of the synthesized beam area. Using the astrodendro results as the initial input, we performed a final 2D Gaussian fit to each of the identified cores using the Cube Analysis and Rendering Tool for Astronomy (CARTA; Comrie et al. 2021). We followed the nomenclature for dense cores used in Shepherd et al. (2003) and Rodríguez-Kamenetzky et al. (2020). The mask for the entire cloud and the FWHM ellipses representing the dense cores are shown in Figure 1(b). Table 2 lists the observation parameters for those structures. The paremeters for the "all" mask are from astrodendro, and the equivalent FWHMs are calculated from the intensity-weighted second moment in the corresponding directions. The parameters of the dense cores are from CARTA.

Assuming that the cloud is isothermal, the continuum emission is optically thin, and the gas-to-dust mass ratio is a constant $\Lambda = 100$, we can derive the total mass of the structures using the observed integrated flux of the dust emission, F_ν, by

$$M = \frac{\Lambda F_\nu D^2}{B_\nu(T_d)\kappa_\nu}, \quad (1)$$

where $D = 1.3$ kpc is the distance to the source, $\kappa_\nu = (\nu/1000\,\mathrm{GHz})^\beta$ m^2 kg^{-1} is the dust opacity (Hildebrand 1983), and $B_\nu(T_d)$ is the Planck function at a given dust temperature T_d. We utilized an opacity index of $\beta = 1.5$ (Pollack et al. 1994; Beuther et al. 2007; Chen et al. 2007), and the average T_d within each dense structure in W75N was listed in Table 3 from ammonia hyperfine line fitting using EVLA data (X. Zhang et al. 2023, in preparation). While the fittings for MM2 and MM3 did not converge, we were still able to estimate the temperatures to be between 30 and 45 K, and hence we used $T_d = 45$ K to determine the lower limits for the mass. The average density, column density $N_{\mathrm{H_2}}$, and volume density $n_{\mathrm{H_2}}$ within each structure are calculated as

$$\rho = \frac{3M}{4\pi r^3}, \quad (2)$$

$$N_{\mathrm{H_2}} = \frac{M}{\pi m_{\mathrm{H}} \mu_{\mathrm{H_2}} r^2}, \quad (3)$$

$$n_{\mathrm{H_2}} = \frac{3M}{4\pi m_{\mathrm{H}} \mu_{\mathrm{H_2}} r^3}, \quad (4)$$

[8] http://www.dendrograms.org/

Table 3
Fitting Parameters of Dense Structures

Structure	T_d (K)	M ($M_\odot$)	ρ (10^{-15} kg m^{-3})	$N_{\mathrm{H_2}}$ (10^{23} cm^{-2})	$n_{\mathrm{H_2}}$ (10^6 cm^{-3})
all	63	35.5	4.1	1.8	0.85
MM1	73	17.1	11.2	2.8	2.3
MM2	<45	8.9	9.2	2.0	1.9
MM3	<45	3.4	5.6	1.0	1.2
MM4	58	5.0	2.8	0.73	0.58
MM[N]	45	3.1	3.0	0.67	0.63

where $r = \sqrt{(\mathrm{FWHM}_a \times \mathrm{FWHM}_b)}$ (Motte et al. 2007) is the geometric mean radius of the structure, $\mu_{\mathrm{H_2}} = 2.86$ is the mean hydrogen molecular weight (Kirk et al. 2013; Pattle et al. 2015), and m_{H} is the hydrogen atomic mass. The mass, average density, column density, and volume density of the dense structures derived from Equations (1) to (4) are listed in Table 3. The estimated column and volume densities of the structures in W75N are generally similar to those in other massive star-forming regions.

The uncertainties in the parameters discussed above arise from various sources. The characterization of the constant Λ and κ_ν is not well constrained and contributes to an uncertainty over 50% (Draine 2011; Beuther et al. 2018) and a factor of 2 (Ossenkopf & Henning 1994; Motte et al. 2007), respectively. The ammonia line data yield dust temperatures ranging from 30 to 73 K, consistent with the results of Shepherd (2001), which estimated temperatures of 35–75 K. For MM2 and MM3, we estimated the lower mass limits using the upper fitting temperatures. The distance to W75N, as estimated by Rygl et al. (2012), is uncertain by approximately 5%. As a result, the final uncertainties for the mass, density, column density, and volume density listed in Table 3 are estimated to be at least a factor of 2.1.

3.2. Dust Polarization

Since polarized intensity and polarized percentage are defined as positive values, the measurements of these two parameters tend to be biased toward larger values. In order to correct for this bias, the debiased polarized intensity (PI) can be calculated using the following formula (Vaillancourt 2006):

$$\mathrm{PI} = \sqrt{Q^2 + U^2 - 0.5(\sigma_Q^2 + \sigma_U^2)}, \quad (5)$$

where σ_Q and σ_U are the 1σ rms noise of the Q and U maps. The polarization fraction is calculated as

$$\mathrm{Pf} = \mathrm{PI}/\mathrm{I}, \quad (6)$$

where I is the Stokes I intensity.

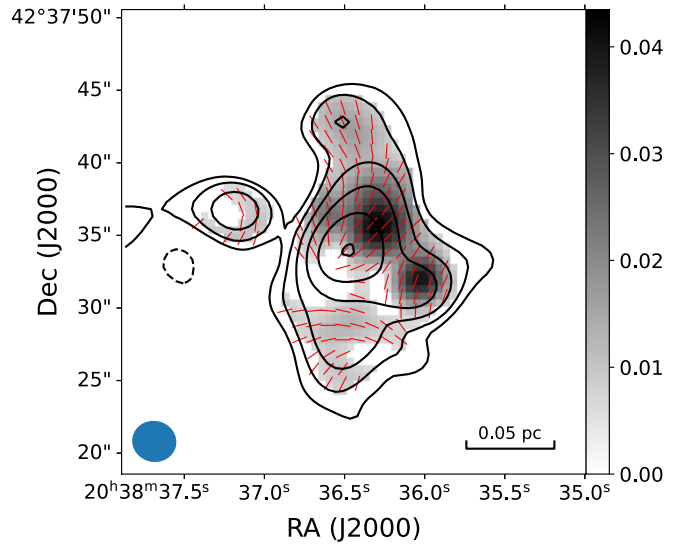

Figure 2. W75N magnetic field orientation map. Polarized emission intensities are shown in gray scales in the units of Jy beam^{-1}. Magnetic field orientations inferred from the linearly polarized emission with PI/$\sigma_{\rm PI} > 3$ are shown as red line segments. Intensity contour levels are the same as those in Figure 1.

Assuming that irregular grains have their shortest axis aligned with the magnetic field lines (Lazarian 2007; Lazarian & Hoang 2007; Andersson et al. 2015), we can determine the magnetic field orientation projected on the plane of sky (POS) by rotating the polarization segments by 90°. Figure 2 displays the magnetic field orientations overlaid on the polarization intensity map, where two polarization intensity peaks are observed, one close to MM2 and the other to the northwest of MM1. As shown in Figure 3, the magnetic field orientation distribution falls into three major groups. The first group with position angles between 0° and 40° is dominated by the polarized emission from MM[N], while the second group with position angles between 60° and 120° is mainly associated with the polarized emission from MM4. The last group comprises detections from the polarization intensity peaks around MM1 and MM2, with polarization angles from 130° to 180°. As these groups are found to be related to the dense structures described in Section 3.1, the magnetic field angles can be assumed to be uniform within each dense structure.

In Figure 4, we present the polarization fraction (Pf) as a function of I for the entire W75N region. We then fitted the Pf–I relation using a simple power law of $P \propto I^{\alpha}$, with an estimated index of $\alpha = -0.4 \pm 0.3$. This relation can be used to evaluate the grain alignment efficiency within a cloud. In more developed star-forming regions, the alignment efficiency is often enhanced by additional radiation, resulting in a power-law index with a smaller absolute value (the slope is shallower) in the Pf–I relation.

3.3. Magnetic Field Analysis

The Davis–Chandrasekhar–Fermi (DCF) method (Davis 1951; Chandrasekhar & Fermi 1953) relates the dispersion of polarization position angles to the large-scale mean magnetic field strength. This analysis tool has been widely used to obtain the strength of the magnetic field projected on the POS. We refer readers to Liu et al. (2022b) for a review and detailed discussion of the assumptions in the DCF analysis. Further studies have been made to expand the DCF

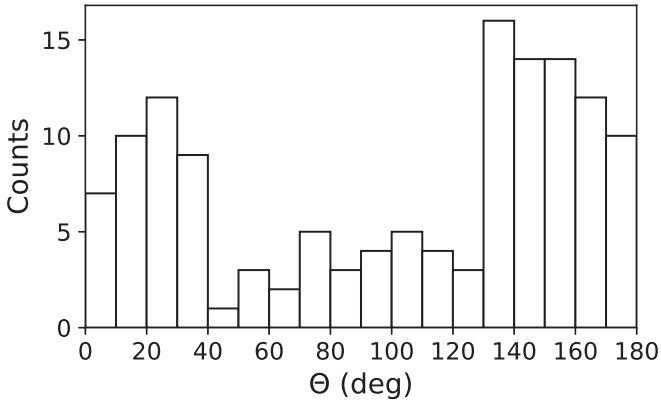

Figure 3. Histogram of position angles of the magnetic field segments from Figure 2. The bin size is 10°, and position angles are measured east of north.

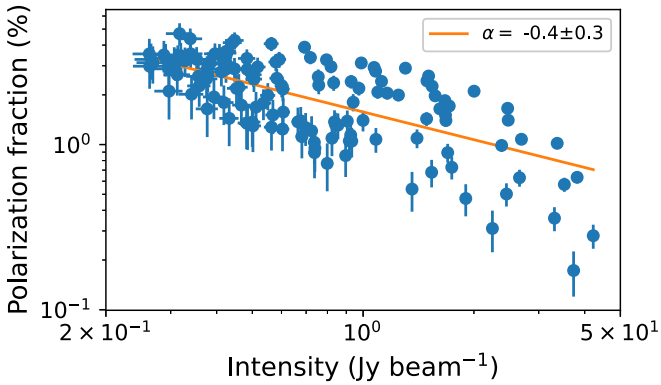

Figure 4. Polarization percentage vs. Stokes I plots. Polarization data points from Figure 2 are shown in log–log scale with error bars. The orange line shows the fitting results using the power-law model.

method using the angular dispersion function (ADF) analysis (Falceta-Gonçalves et al. 2008; Hildebrand et al. 2009; Houde et al. 2009, 2011, 2016). Specifically, using the twin Gaussian model for the interferometer beams, Houde et al. (2016) derived the angular dispersion solutions for the interferometer, which can be expressed as Equation (13) in their work. We can rewrite it as

$$1 - \langle \cos[\Delta\phi(\ell)] \rangle = \sum_{j=1}^{\infty} a_{2j} \ell^{2j} + \frac{1}{1 + N \langle B_0^2 \rangle / \langle B_t^2 \rangle} - b^2(\ell), \tag{7}$$

where $\Delta\phi(\ell)$ is the angular difference of the two polarization segments separated by a distance of ℓ, N is the number of the turbulent cells, $\langle B_0^2 \rangle / \langle B_t^2 \rangle$ is the large-scale to turbulent magnetic strength ratio, and $b^2(\ell)$ is the local turbulent component of the ADF. The contribution of the large-scale component to the dispersion function can be written as $1 - \langle \cos[\Delta\phi(\ell)] \rangle - b^2(\ell)$. Assuming the turbulent correlation length is δ, the effective thickness of the observation region is Δ', and the beam sizes (standard deviation) of the twin Gaussian model are W_1 and W_2, N and $b^2(\ell)$ can be written as

$$N_1 = \frac{(\delta^2 + 2W_1^2)\Delta'}{\sqrt{2\pi}\,\delta^3}, \tag{8}$$

$$N_2 = \frac{(\delta^2 + 2W_2^2)\Delta'}{\sqrt{2\pi}\,\delta^3}, \tag{9}$$

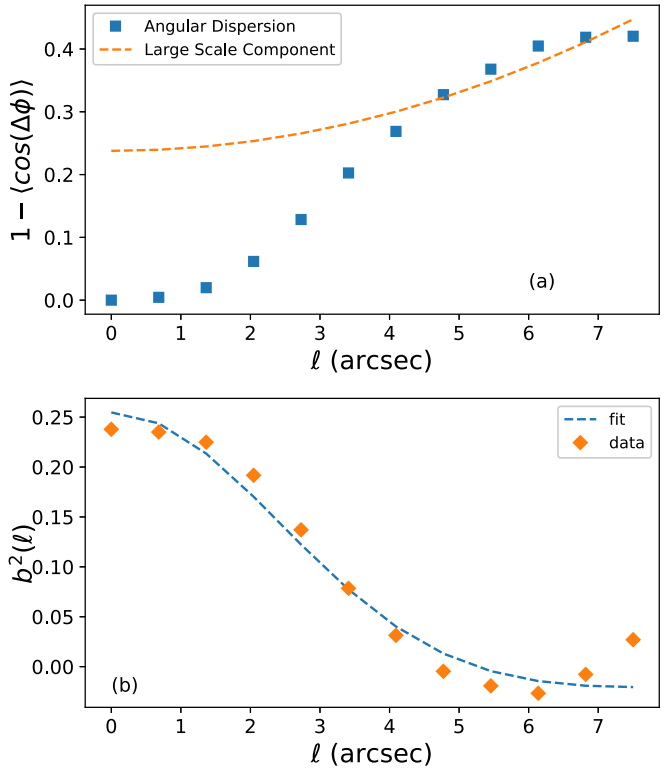

Figure 5. Dispersion function $1 - \langle\cos(\Delta\phi)\rangle$ for W75N using the 345 GHz SMA data. (a) Angular dispersion data (symbols) plotted as a function of distance ℓ; the dashed curve from Gaussian fitting represents contribution from the large-scale component. (b) The resulting turbulence correlation function $b^2(\ell)$ and its fitting curve.

$$N_{12} = \frac{(\delta^2 + W_1^2 + W_2^2)\Delta'}{\sqrt{2\pi}\,\delta^3}, \tag{10}$$

$$N = (1/N_1 + 1/N_2 - 2/N_{12})^{-1}, \tag{11}$$

$$b^2(\ell) = \frac{N}{1 + N\langle B_0^2\rangle/\langle B_t^2\rangle}\left\{\frac{1}{N_1}e^{-\ell^2/[2(\delta^2+2W_1^2)]} + \frac{1}{N_2}e^{-\ell^2/[2(\delta^2+2W_2^2)]} - \frac{1}{N_{12}}e^{-\ell^2/[2(\delta^2+W_1^2+W_2^2)]}\right\}. \tag{12}$$

Due to the limited number of detected polarization segments, performing the angular dispersion analysis on each dense structure in the W75N region is impractical. Therefore, we estimated the mean magnetic field (B_0) for the entire cloud by utilizing the position angle data from the polarization measurements presented in Figure 2. For the twin Gaussian beam sizes, the telescope beam width radius W_1 can be estimated using the size of the synthesized beam, $W_1 = \sqrt{\mathrm{FWHM}_a^{\mathrm{beam}} \times \mathrm{FWHM}_b^{\mathrm{beam}}}/(\sqrt{8\ln 2})$, and W_2 is the resolution calculated from the shortest baseline of the array. For our analysis, we set $W_1 = 1\farcs2$ and $W_2 = 8\farcs0$. We determined the effective thickness of the cloud to be the ratio of the volume to the cross area of the equivalent sphere of the entire cloud:

$$\Delta' = V/A = (4/3)\pi r^3/(\pi r^2) = 4r/3 = 11\farcs0, \tag{13}$$

where $r = \sqrt{(\mathrm{FWHM}_a \times \mathrm{FWHM}_b)} = 8\farcs2$. With the parameters outlined above, we plotted the derived W75N polarization angular dispersion data and fittings in Figure 5. We fitted the data points between $4'' < \ell < 8''$, as scales below $\ell < 4''$, were smaller than our synthesized beam. We set the upper fitting boundary at $\ell \approx 8''$, as Equation (7) is valid when ℓ is less than a few times the beam size (W_1; Houde et al. 2009). Our fitting results yielded the turbulent-to-total magnetic energy ratio, $\langle B_t^2\rangle/\langle B_0^2\rangle = 2.1 \pm 0.7$, and $\delta = 1\farcs7 \pm 0\farcs2$. The large-scale magnetic field strength was estimated as (Houde et al. 2009)

$$B_0 = \sqrt{\mu_0\rho}\,\frac{\delta\nu}{\delta\theta} = \sqrt{\mu_0\rho}\,\delta\nu\left[\frac{\langle B_t^2\rangle}{\langle B_0^2\rangle}\right]^{-1/2} = 0.8 \pm 0.1\ \mathrm{mG}, \tag{14}$$

where μ_0 is the vacuum permeability, ρ is the average density of the cloud, and $\delta\nu = 1.5$ km s^{-1} is the turbulent velocity dispersion in the cloud, which was estimated from the $H^{13}CO^+$ (4–3) line-of-sight (LOS) velocity dispersion (see Section 3.5).

Previous studies have revealed that the W75N cloud is linked to the DR21 region, and both regions are in a comparable global collapse state as a result of converging flows on large scales (Schneider et al. 2010). Magnetic field strength measurements of DR21 cores from earlier observations range from 0.4 to 2.1 mG (Girart et al. 2013; Ching et al. 2017), which is consistent with the magnetic field strength derived in this study for W75N.

The Alfvénic Mach number (M_A), the sonic Mach number (M_s), and the ratio of thermal-to-magnetic pressures (β) of the cloud can be calculated as

$$M_A = \sqrt{3}\,\delta\nu/\nu_A, \tag{15}$$

$$M_s = \sqrt{3}\,\delta\nu/c_s, \tag{16}$$

$$\beta = 2(M_A/M_s)^2 = 2(c_s/\nu_A)^2, \tag{17}$$

where $\delta\nu = \delta\nu_{\mathrm{los}}$ is the 1D velocity dispersion, $\nu_A = B_0/\sqrt{\mu_0\rho}$ is the Alfvénic velocity, and $c_s = \sqrt{\gamma k_B T/(\mu m_H)}$ is the sound speed at temperature T using the adiabatic index $\gamma = 5/3$ and the mean molecular weight $\mu = 2.33$. With the average cloud temperature of 63 K, we calculated $c_s = 0.61$ km s^{-1}. ν_A is calculated to be 1.0 km s^{-1}, and the corresponding β value is 0.7. The calculated M_A, M_s, and β values for the cloud are listed in Table 4.

Table 4
Viral Parameters of W75N

$\delta\nu_{\mathrm{los}}$/(km s^{-1})	M_s	M_A	β	β_{turb}	λ	χ
1.5	5.6	3.3	0.7	10.9	2.0	3.5

3.4. Polarization—Intensity Gradient Analysis

Within the framework of ideal magnetohydrodynamics (MHD), and assuming that the intensity gradient traces the direction of gas motion in the MHD force equation, Koch et al. (2012) developed a technique to connect the position angle between polarization and intensity gradient orientations to the total magnetic field strength. Using this technique, we calculated the angular differences between the intensity gradient, the local gravity, and the magnetic field orientation. Figure 6(a) displays the $\sin\psi$-map for pixels with a detection higher than 3σ, where ψ represents the difference between the intensity gradient and local gravity orientations. Assuming that

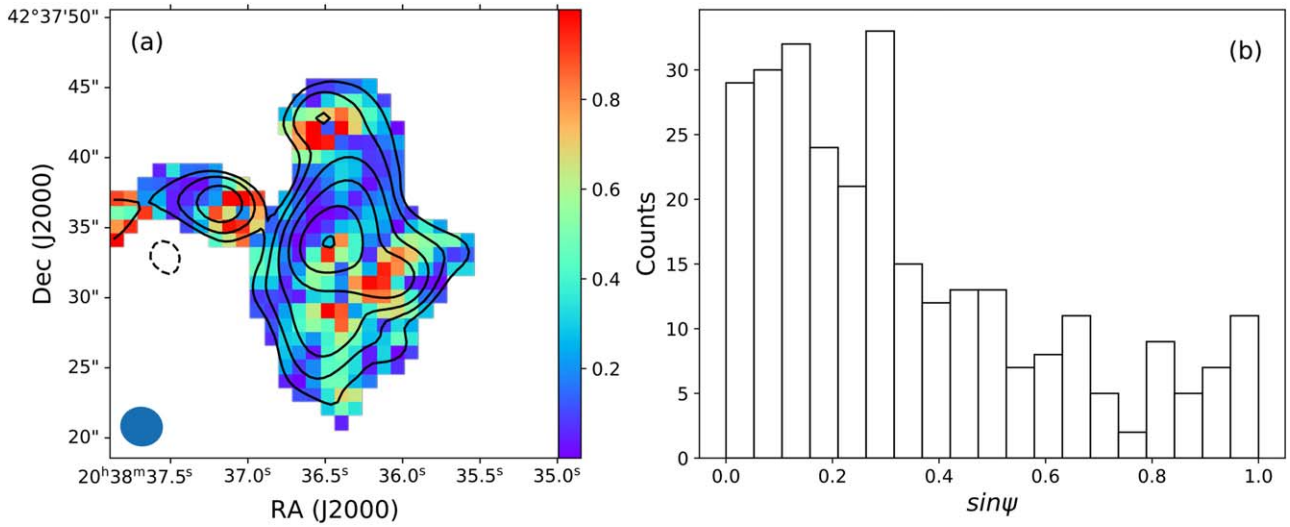

Figure 6. Relevant angles for magnetic field strength derivation. (a) The sin ψ-map, where ψ is the difference between the orientations of the intensity gradient and local gravity. The black curves are the intensity contours as shown in Figure 1. (b) The histogram of sin ψ.

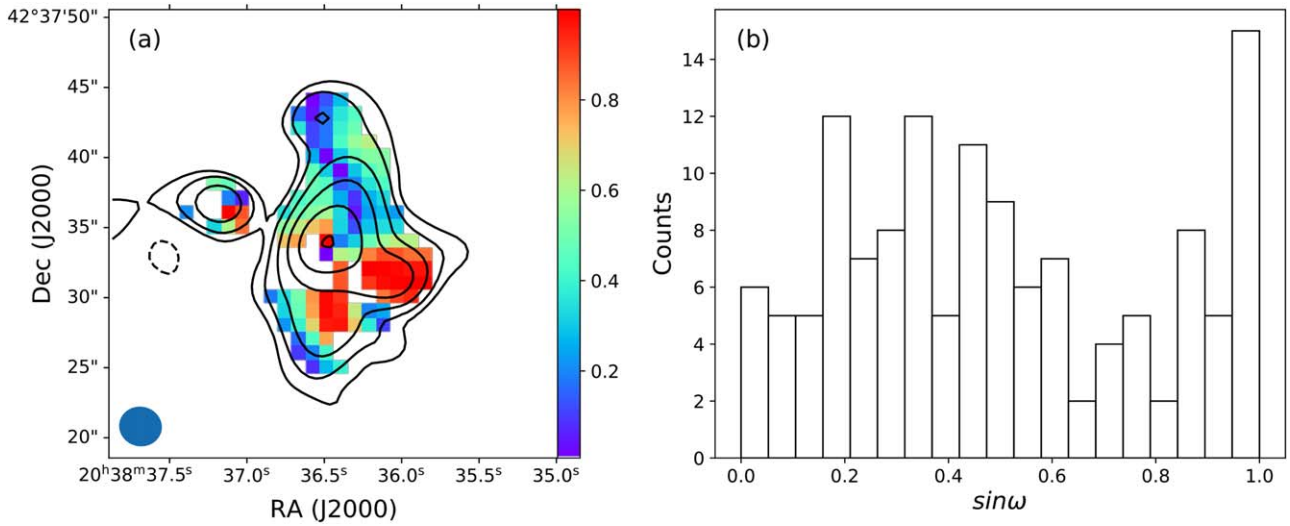

Figure 7. Relevant angles for magnetic field strength derivation. (a) The sin ω-map, where ω is the difference between the magnetic field and local gravity orientations. The black curves are the intensity contours as shown in Figure 1. (b) The histogram of sin ω.

mass is proportional to the detected dust emission intensity, for an intensity map with n positions, the local gravity at a given position $\boldsymbol{r}_i$ can be calculated using the following formula (Koch et al. 2012):

$$\boldsymbol{g}(\boldsymbol{r}_i) \propto \sum_{j=1}^{n} \frac{I_j}{|\boldsymbol{r}_i - \boldsymbol{r}_j|^2} \cdot \boldsymbol{e}_{ji}, \quad (\text{for } j \neq i), \tag{18}$$

where $\boldsymbol{e}_{ji}$ is the unit directional vector between position $\boldsymbol{r}_j$ and $\boldsymbol{r}_i$, and I_j is the continuum intensity at position $\boldsymbol{r}_j$. Figure 6(b) shows that the majority of sin ψ values are small, less than 0.4, indicating that changes in the local intensity structure closely follow the local gravity. Positions with high sin ψ values are mostly situated between intensity peaks, where the local gravity is canceled out in a particular orientation.

The sin ω-map, which displays the difference between the magnetic field and local gravity orientations, is presented in Figure 7(a), and its corresponding histogram is shown in Figure 7(b). The sin ω distribution is characterized by two major peaks, one ranging from 0.2 to 0.5, and the other from 0.8 to 1.0. Regions with low sin ω values, particularly along the MM1 to MM[N] direction, indicate a strong alignment between the magnetic field and local gravity, resulting in a magnetic field morphology that is primarily shaped by gravity. Conversely, regions with high sin ω values, such as those located around the MM2, MM3, and MM4 peaks, suggest that the magnetic field is more dominant.

We also studied the magnetic field magnetic field significance (Σ_B) to evaluate the relative importance of the magnetic field (F_B) in comparison to gravity (F_G) and pressure gradient (F_P) at various locations within the cloud. Σ_B is calculated using the equation

$$\Sigma_B = \frac{F_B}{|F_G + F_P|} = \frac{\sin\psi}{\cos\delta}, \tag{19}$$

where δ represents the difference between the magnetic field and intensity gradient orientations. The resulting Σ_B-map and distribution are depicted in Figure 8.

Based on the results presented in Figures 2 and 7, it appears that the MM[N] region is strongly influenced by the gravity of

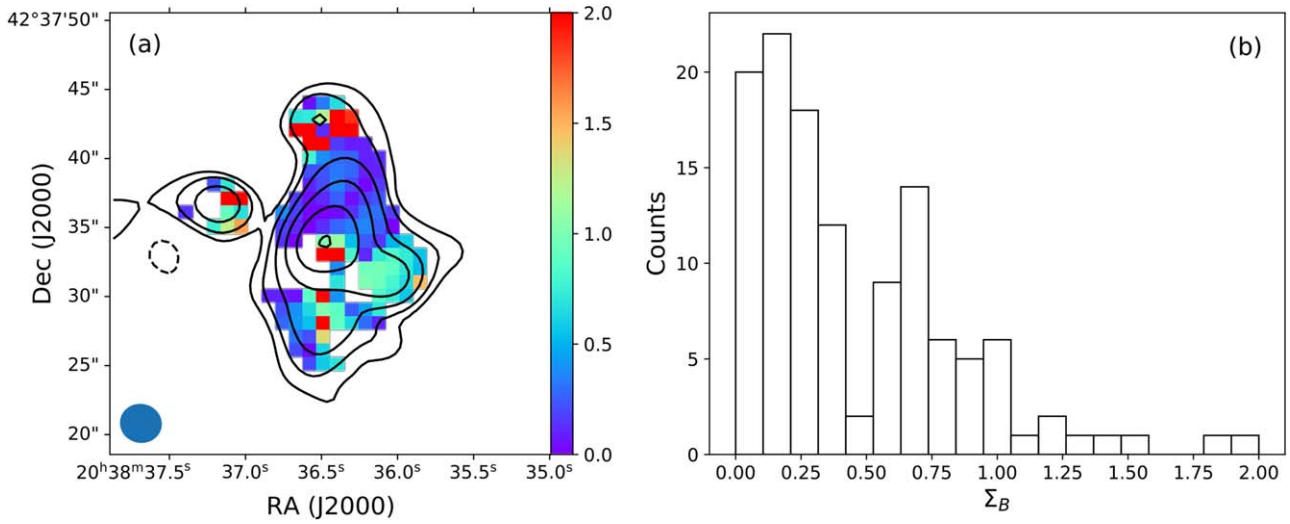

Figure 8. Relevant angles for magnetic field strength derivation. (a) The map of field significance Σ_B. The black curves are the intensity contours as shown in Figure 1. (b) The histogram of Σ_B.

the main MM1 core. This gravity exerts a strong pull on the magnetic field, directing it toward the center of the cloud. Near the MM[N] peak, there is a notable discrepancy between the magnetic field and intensity gradient orientations. We conclude that the MM[N] core is a low-mass structure that is dominated by the gravity of the nearby high-mass core (MM1), similar to the case of "Region IV" in Koch et al. (2012). In such scenarios, the basic assumption that the intensity gradient traces the gas motion direction does not hold strictly, leading to high uncertainties. The Σ_B values are dominated by large changes in ψ when linked to the gravitational center of the main core. Given the lack of a clear identification of a local gravity center, the calculated ψ values may be much smaller, resulting in overestimated Σ_B values in the region, which are shown in Figure 8.

If we ignore the Σ_B values near the MM[N] region, the majority of the Σ_B values are below 1.0, particularly in the northern MM1 region, indicating that the cloud is experiencing global collapse, with the magnetic field being unable to balance the gravitational and pressure forces. Conversely, in the MM3 and MM4 core regions, the Σ_B values are higher, suggesting that the magnetic field may be more dominant. Around the MM2 peak, the value is approximately 1, indicating that the magnetic force is comparable to the other forces.

3.5. Molecular Line Emission Analysis

The kinematic information on the gas dynamics in the star-forming clouds enables us to probe the star formation scenario. Utilizing data from the $H^{13}CO^+$ (4–3) line emission, which is optically thin and devoid of self-absorption features, enables us to estimate the physical parameters of the dense cores in W75N. Figure 9 illustrates the moment 1 map of the $H^{13}CO^+$ (4–3) line emission in color-scale overlay on the continuum contours. The magnetic field orientations are depicted by red segments. The figure shows the contamination of high-velocity components by the outflows, indicated by the redshifted lobes in Figure 11, located to the east and west of the center MM1 region and around MM3. A significant velocity gradient from the MM[N] region to the MM1 core is observed. Based on our analysis in Section 3.4, the W75N cloud is undergoing global collapsing. The observed velocity gradient may be caused by gas flow from MM[N] to MM1 or cloud rotation.

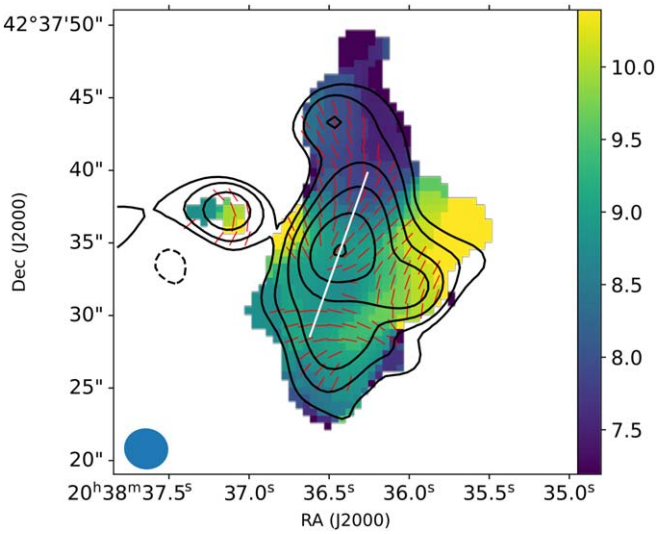

Figure 9. Contour map of the dust emission superposed on the color image of the flux-weighted velocity map (moment 1) of the $H^{13}CO^+$ (4–3) line. The color scale is in units of km s^{-1}. Red segments indicate the directions of the magnetic field. The path in white color shows the slice position on MM1 for position–velocity analysis.

To avoid the contamination from the outflows, we perform the position–velocity (PV) analysis to model the velocity gradient along the vertical white color path (PA = –20°) shown in Figure 9. The PA angle is chosen to be perpendicular to the large-scale outflow shown in Figure 11 and is consistent with the disk-like structure unidentified by Hutawarakorn et al. (2002) and van der Walt et al. (2021). The ellipse resulting from the best 2D Gaussian fit, represented in Figure 10, indicates a slope angle of 24° and a calculated velocity gradient of approximately 0.9 km s^{-1} $arcsec^{-1}$. If the observed gradient is due to cloud rotation, it corresponds to a rotation velocity of $\omega = 1.4 \times 10^{-4}$ yr^{-1}, resulting in $(\omega/B)_{obs} = 1.7 \times 10^{-7}$ yr^{-1} μG^{-1}. Depending on the magnetic field strength and rotation velocity, the evolution of a collapsing dense core can be regulated either by centrifugal forces or magnetic forces. We

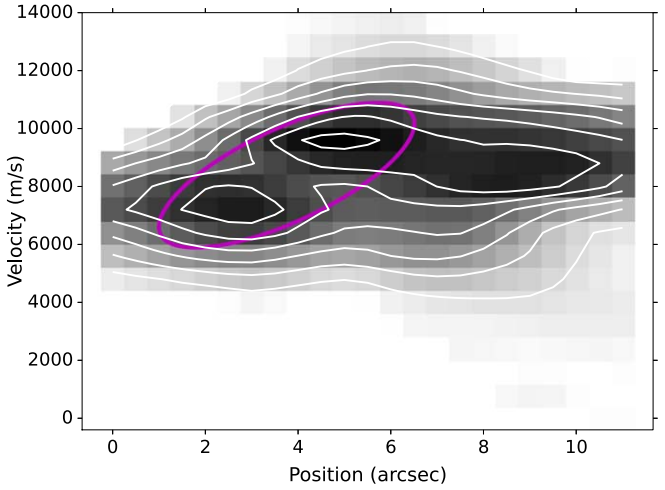

Figure 10. Position–velocity map of the center region from the slice path shown in Figure 9. The purple ellipse shows the best fit to velocity gradient.

define a centrifugal critical parameter χ, which is the ratio of the observed $(\omega/B)_{\rm obs}$ to the critical $(\omega/B)_{\rm crit}$ (Machida et al. 2005):

$$\chi = \frac{(\omega/B)_{\rm obs}}{(\omega/B)_{\rm crit}} = \frac{(\omega/B)_{\rm obs}}{1.69 \times 10^{-7}(c_s/0.19\ {\rm km\ s^{-1}})^{-1}{\rm yr}^{-1}\,\mu{\rm G}^{-1}}. \quad (20)$$

Given $c_s = 0.61$ km s^{-1}, $(\omega/B)_{\rm crit}$ is calculated to be 5.3×10^{-8} yr^{-1} μG^{-1} and the χ value for the cloud is 3.5, which is greater than 1. The centrifugal forces dominate the dynamics of the collapse over the magnetic field.

We determined the turbulent velocity dispersion, $\delta v_{\rm los}$, by fitting the line width of the $H^{13}CO^+$ (4–3) spectrum. Since the molecular weight is high and T_d (temperature) is low, the impact of thermal velocity dispersion is negligible. To eliminate the contribution of large-scale velocity motion within the cloud, we applied a method that shifts the velocity of a spectrum for each spatial pixel by the centroid velocity indicated in the moment 1 map (refer to Figure 9) to remove the large-scale velocity field. This technique shifts the average velocity of each pixel to zero, isolating only the turbulent component. The turbulent velocity is then determined by fitting a Gaussian profile to the intensity–velocity curve. The final estimated value for $\delta v_{\rm los}$ is approximately 1.5 km s^{-1}.

The ratio of the turbulent to magnetic energy $\beta_{\rm turb}$ is usually calculated using the Alfvénic Mach number:

$$\beta_{\rm turb} = M_{\rm A}^2 = 3(\delta v_{\rm los}/v_{\rm A})^2. \quad (21)$$

The $\beta_{\rm turb}$ for the entire cloud is calculated to be 10.9, indicating the turbulent energy dominates the magnetic energy.

The relative importance between the magnetic field and the gravity of individual sources can be estimated by the magnetic critical parameter λ, which is the mass-to-flux ratio in units of the critical value $1/(2\pi\sqrt{G})$ (Mouschovias & Spitzer 1976; Nakano & Nakamura 1978; Crutcher 2004):

$$\lambda = \frac{(M/\Phi_B)_{\rm obs}}{(M/\Phi_B)_{\rm ntextcrit}} = 7.6 \times 10^{-21}\frac{N_{\rm H_2}/({\rm cm}^{-2})}{B/(\mu{\rm G})}. \quad (22)$$

The calculated λ value for W75N is about 2.0, indicating gravity dominates the magnetic field.

Table 4 lists the viral parameters of W75N. The cloud has $M_s > 1$, revealing that nonthermal motions are supersonic. The $M_{\rm A}$ value is greater than 1, indicating that turbulent energy is stronger than magnetic energy. These supersonic and super-Alfvénic Mach numbers imply the presence of strong nonthermal motions in the cloud. The β value is less than 1, indicating that although weaker than the nonthermal pressure, the magnetic pressure is stronger than the thermal pressure. This $M_s > M_{\rm A} > 1 > \beta$ relationship has been previously observed in other high-mass forming regions, such as the DR21 cores (Ching et al. 2017).

The average λ value for the cloud is 2.0, indicating it is undergoing a global collapse. The estimated B_0 and λ values in this work are consistent with the results ($B_0 = 0.3$–1.2 mG and $\lambda = 0.6$–2.2) obtained by Palau et al. (2021). The cloud exhibits a large-scale velocity gradient, but it is unclear whether it is due to gas infall or cloud rotation. If the cloud is rotating, the high χ value suggests that the centrifugal force dominates the magnetic field force.

4. Discussion

Observations of the Zeeman effect toward maser sources at small scales have been used to derive magnetic field strengths in the LOS direction. The magnetic field strength derived from Zeeman pairs of opposite circular polarization ranges from +8 to −8 mG using OH masers at 1665, 1667, and 1720 MHz (Hutawarakorn et al. 2002). Fish & Reid (2007) detected a strong magnetic field source of about 40 mG near VLA 2. Surcis et al. (2009) observed the 6.7 GHz methanol maser using the European VLBI network and found that the Zeeman-splitting measurements indicated the LOS magnetic fields in the maser regions ranging from 11 to 16 mG. In contrast, the magnetic field strength measured from observations of the 22 GHz water masers is about 1000 mG (Surcis et al. 2011), which is much higher than those from the methanol maser observations. Recently, Surcis et al. (2023) measured –764 mG $< B^{\rm VLA1} <$ –676 mG and –355 mG $< B^{\rm VLA2} <$ –2426 mG in the LOS direction with 22 GHz water maser observations. These high-resolution (typically around 10^2 au) maser observations detected much higher LOS magnetic field strengths at small scales in protostellar envelopes. The hydrogen number densities of those regions estimated using the empirical equation $B \propto n_{\rm H_2}^{0.65}$ (Crutcher et al. 2010) range from 10^8 to 10^{10} cm^{-3} (Surcis et al. 2023). It is not straightforward to compare the results from our work using thermal dust emission to those from maser observations arising from nonthermal processes. Based on the findings from Liu et al. (2022a), the density and magnetic field strength (0.85×10^6 cm^{-3} and 0.8 mG) from this work indicate that the cloud is in a magnetically supercritical phase.

Vallee & Bastien (1995) conducted JCMT observations toward the compact source W75N-IRS1 using a beam size of 12″ at 870 μm. They detected one magnetic segment with a PA $= 145° \pm 5°$ and estimated a magnetic field strength of $B = 0.8$ mG using a simple statistical relation between the magnetic field strength and the gas density. Their magnetic field strength and PA are consistent with the mean field of our results. Using JCMT, Greaves & Holland (1998) obtained a similar magnetic field position angle of $153° \pm 22°$ at 1100 μm, while at 450 μm, the derived magnetic field was $37° \pm 9°$. The change in magnetic field PA could be attributed to the twisted magnetic field lines around the region. The net magnetic field

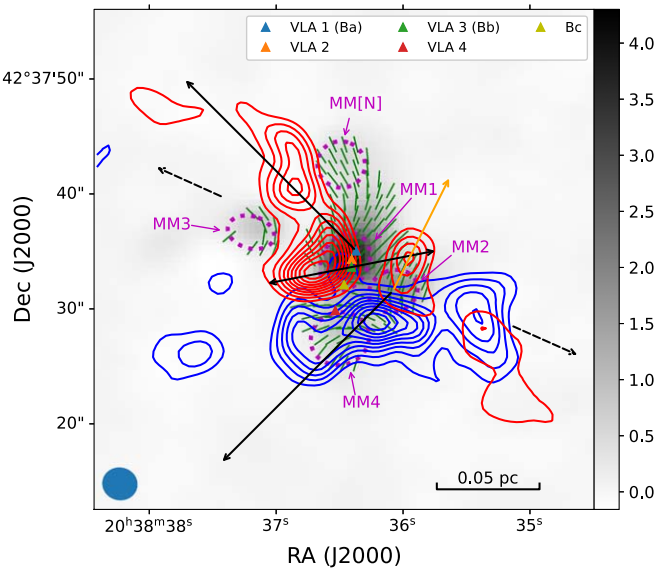

Figure 11. Integrated CO (3–2) blueshifted and redshifted emission contours from −18.0 to 0 km s^{-1} and 20.0 to 28.0 km s^{-1}, respectively. The peaks for the blueshifted and redshifted emission are 275.3 mJy beam^{-1} km s^{-1} and 191.6 mJy beam^{-1} km s^{-1}. Contours begin at 10% of the peak emission and continue at increments of 10%. The continuum emission shown in background is identical to that in Figure 1. The two dashed arrows indicated the direction of the bipolar outflow from Hunter et al. (1994). The three solid arrows are from Shepherd et al. (2003). Compact sources are labeled as filled triangles. The green segments are the magnetic field from Figure 2. The dashed ellipses in magenta show the dense cores from Figure 1(b).

value could change as the beam size varies. Similarly, the maser observations obtained magnetic fields perpendicular to our submillimeter polarization observations because the maser observations were at milliarcsecond (mas) resolution to trace the compact H II regions. The magnetic field could twist significantly from mas to arcsecond scales.

In Figure 11, we present the CO (3–2) blueshifted and redshifted emission contours from our work. We chose the velocity boundaries of the blueshifted (−18.0 to 0 km s^{-1}) and redshifted (20.0–28.0 km s^{-1}) emissions to be symmetrical with respect to the cloud's $\nu_{\rm LSR}$ = 10.0 km s^{-1}, as reported by Shepherd et al. (2003). The compact sources VLA 1 (Ba), VLA 2, VLA 3 (Bb), Bc, and VLA 4 are marked as filled triangles, and the dense cores of the cloud from Figure 1 are labeled using dashed ellipses. The black dashed arrows indicate the direction of the bipolar outflow (66°) from Hunter et al. (1994), and the three black solid arrows from Shepherd et al. (2003) show the outflow orientations for the redshifted component (45°, started from VLA 1), blueshifted component (135°, started from MM2), and the bipolar outflow from VLA 3 (101°, centered at VLA 3). Torrelles et al. (1997) and Surcis et al. (2009) also suggested that VLA 1 powers the large-scale molecular bipolar outflow of W75N(B).

We found that the main outflows centered at VLA 1 and MM2 from Shepherd et al. (2003) match well with the high-velocity gas detected in our CO (3–2) emission map. However, we did not detect the blueshifted components of the bipolar outflows from VLA 3 to the west of the source. We propose the existence of another outflow centered at MM2, extending in a direction almost opposite to that of MM4, indicated by the orange arrow in Figure 11. The bipolar outflows originating from the MM2 core drag and align the magnetic field lines in the MM2 and MM4 regions. In addition, we found enhanced dust polarization along the cavity walls of the redshifted lobe of the outflow, specifically around the MM3 region. The magnetic field lines in the MM[N] and MM1 regions are shaped by gas infall from the MM[N] to MM1 core. These findings are consistent with the results of the polarization angle analysis presented in Section 3.2.

The overall λ is greater than 1, and the Σ_B values shown in Figure 8(b) predominantly fall below 1, indicating that the W75N cloud is undergoing global collapsing. In the MM2 and MM4 regions, while the Σ_B values increase, they still remain primarily below 1, as these regions are dominated by gravity and pressure gradient. The magnetic field is also shaped by the outflows from the MM2 core. If the large-scale velocity is from cloud rotation, the average cloud $M_{\rm A}$ = 3.3 and χ = 3.5, indicating that turbulence and the centrifugal force dominate over magnetic field.

5. Conclusion

We present 345 GHz polarization observations of the W75N region using the SMA interferometer. We estimated the physical parameters of the dense structures in the region from the dust continuum emission. Our analysis reveals a uniform distribution of polarization angles within each dense structure. We used the ADF method to study the POS magnetic field and estimated a large-scale magnetic field component of 0.8 ± 0.1 mG. We also investigated the dynamical state of the cloud by analyzing the polarization-intensity gradient and the $H^{13}CO^+$ (4–3) line data. Our findings suggest that the W75N region is undergoing global collapsing due to the weaker magnetic field force compared to other forces. We observed that the magnetic field around the MM[N] and MM1 regions is aligned by gas infall, while in the MM2 and MM4 regions, the magnetic field is shaped by outflows from the MM2 core. We also observed enhanced dust polarization along the cavity walls around the MM3 region.

Acknowledgments

This work was partially supported by the program Unidad de Excelencia María de Maeztu CEX 2020-001058-M. J.G. also acknowledges support by the grant PID 2020-117710 GB-I00 (MCI-AEI-FEDER,UE).

ORCID iDs

Lingzhen Zeng https://orcid.org/0000-0001-6924-9072
Qizhou Zhang https://orcid.org/0000-0003-2384-6589
Felipe O. Alves https://orcid.org/0000-0002-7945-064X
Tao-Chung Ching https://orcid.org/0000-0001-8516-2532
Josep M. Girart https://orcid.org/0000-0002-3829-5591
Junhao Liu https://orcid.org/0000-0002-4774-2998

References

Andersson, B. G., Lazarian, A., & Vaillancourt, J. E. 2015, ARA&A, 53, 501
Astropy Collaboration, Price-Whelan, A. M., Sipőcz, B. M., et al. 2018, AJ, 156, 123
Astropy Collaboration, Robitaille, T. P., Tollerud, E. J., et al. 2013, A&A, 558, A33
Beuther, H., Leurini, S., Schilke, P., et al. 2007, A&A, 466, 1065
Beuther, H., Mottram, J. C., Ahmadi, A., et al. 2018, A&A, 617, A100
Carrasco-González, C., Rodríguez, L. F., Torrelles, J. M., Anglada, G., & González-Martín, O. 2010, AJ, 139, 2433
Carrasco-González, C., Torrelles, J. M., Cantó, J., et al. 2015, Sci, 348, 114
Chandrasekhar, S., & Fermi, E. 1953, ApJ, 118, 113

Chen, H.-R., Su, Y.-N., Liu, S.-Y., et al. 2007, ApJL, 654, L87
Ching, T.-C., Lai, S.-P., Zhang, Q., et al. 2017, ApJ, 838, 121
Comrie, A., Wang, K.-S., Hsu, S.-C., et al. 2021, CARTA: Cube Analysis and Rendering Tool for Astronomy, Astrophysics Source Code Library, ascl:2103.031
Crutcher, R. M. 2004, Ap&SS, 292, 225
Crutcher, R. M., Wandelt, B., Heiles, C., Falgarone, E., & Troland, T. H. 2010, ApJ, 725, 466
Davis, L. 1951, PhRv, 81, 890
Draine, B. T. 2011, Physics of the Interstellar and Intergalactic Medium (Princeton, NJ: Princeton Univ. Press)
Eisloffel, J., Mundt, R., Ray, T. P., & Rodriguez, L. F. 2000, in Protostars and Planets IV, ed. V. Mannings, A. P. Boss, & S. S. Russell (Tucson, AZ: Univ. Arizona Press), 815
Falceta-Gonçalves, D., Lazarian, A., & Kowal, G. 2008, ApJ, 679, 537
Federrath, C., Roman-Duval, J., Klessen, R. S., Schmidt, W., & Mac Low, M. M. 2010, A&A, 512, A81
Fish, V. L., & Reid, M. J. 2007, ApJ, 656, 952
Girart, J. M., Frau, P., Zhang, Q., et al. 2013, ApJ, 772, 69
Greaves, J. S., & Holland, W. S. 1998, A&A, 333, L23
Haschick, A. D., Reid, M. J., Burke, B. F., Moran, J. M., & Miller, G. 1981, ApJ, 244, 76
Hennebelle, P., & Chabrier, G. 2009, ApJ, 702, 1428
Hildebrand, R. H. 1983, QJRAS, 24, 267
Hildebrand, R. H., Kirby, L., Dotson, J. L., Houde, M., & Vaillancourt, J. E. 2009, ApJ, 696, 567
Ho, P. T. P., Moran, J. M., & Lo, K. Y. 2004, ApJL, 616, L1
Houde, M., Hull, C. L. H., Plambeck, R. L., Vaillancourt, J. E., & Hildebrand, R. H. 2016, ApJ, 820, 38
Houde, M., Rao, R., Vaillancourt, J. E., & Hildebrand, R. H. 2011, ApJ, 733, 109
Houde, M., Vaillancourt, J. E., Hildebrand, R. H., Chitsazzadeh, S., & Kirby, L. 2009, ApJ, 706, 1504
Hull, C. L. H., & Zhang, Q. 2019, FrASS, 6, 3
Hunter, T. R., Taylor, G. B., Felli, M., & Tofani, G. 1994, A&A, 284, 215
Hutawarakorn, B., Cohen, R. J., & Brebner, G. C. 2002, MNRAS, 330, 349
Kim, J.-S., Kim, S.-W., Kurayama, T., et al. 2013, ApJ, 767, 86
Kirk, J. M., Ward-Thompson, D., Palmeirim, P., et al. 2013, MNRAS, 432, 1424
Koch, P. M., Tang, Y.-W., & Ho, P. T. P. 2012, ApJ, 747, 79
Lazarian, A. 2007, JQSRT, 106, 225
Lazarian, A., & Hoang, T. 2007, MNRAS, 378, 910
Liu, J., Qiu, K., & Zhang, Q. 2022a, ApJ, 925, 30
Liu, J., Zhang, Q., & Qiu, K. 2022b, FrASS, 9, 943556
Machida, M. N., Matsumoto, T., Tomisaka, K., & Hanawa, T. 2005, MNRAS, 362, 369
Menon, S. H., Federrath, C., & Kuiper, R. 2020, MNRAS, 493, 4643
Minh, Y. C., Su, Y. N., Chen, H. R., et al. 2010, ApJ, 723, 1231
Motte, F., Bontemps, S., Schilke, P., et al. 2007, A&A, 476, 1243
Mouschovias, T. C., & Spitzer, L. J. 1976, ApJ, 210, 326
Myers, A. T., Klein, R. I., Krumholz, M. R., & McKee, C. F. 2014, MNRAS, 439, 3420
Nakano, T., & Nakamura, T. 1978, PASJ, 30, 671
Ossenkopf, V., & Henning, T. 1994, A&A, 291, 943
Palau, A., Zhang, Q., Girart, J. M., et al. 2021, ApJ, 912, 159
Pattle, K., & Fissel, L. 2019, FrASS, 6, 15
Pattle, K., Fissel, L., Tahani, M., Liu, T., & Ntormousi, E. 2022, arXiv:2203.11179
Pattle, K., Ward-Thompson, D., Kirk, J. M., et al. 2015, MNRAS, 450, 1094
Pollack, J. B., Hollenbach, D., Beckwith, S., et al. 1994, ApJ, 421, 615
Rodríguez-Kamenetzky, A., Carrasco-González, C., Torrelles, J. M., et al. 2020, MNRAS, 496, 3128
Rosolowsky, E. W., Pineda, J. E., Kauffmann, J., & Goodman, A. A. 2008, ApJ, 679, 1338
Rygl, K. L. J., Brunthaler, A., Sanna, A., et al. 2012, A&A, 539, A79
Sault, R. J., Teuben, P. J., & Wright, M. C. H. 1995, in ASP Conf. Ser. 77, Astronomical Data Analysis Software and Systems IV, ed. R. A. Shaw, H. E. Payne, & J. J. E. Hayes (San Francisco, CA: ASP), 433
Schneider, N., Csengeri, T., Bontemps, S., et al. 2010, A&A, 520, A49
Scoville, N. Z., Carlstrom, J. E., Chandler, C. J., et al. 1993, PASP, 105, 1482
Shepherd, D. S. 2001, ApJ, 546, 345
Shepherd, D. S., Kurtz, S. E., & Testi, L. 2004, ApJ, 601, 952
Shepherd, D. S., Testi, L., & Stark, D. P. 2003, ApJ, 584, 882
Surcis, G., Vlemmings, W. H. T., Curiel, S., et al. 2011, A&A, 527, A48
Surcis, G., Vlemmings, W. H. T., Dodson, R., & van Langevelde, H. J. 2009, A&A, 506, 757
Surcis, G., Vlemmings, W. H. T., Goddi, C., et al. 2023, A&A, 673, 32
Surcis, G., Vlemmings, W. H. T., van Langevelde, H. J., et al. 2014, A&A, 565, L8
Torrelles, J. M., Gómez, J. F., Rodríguez, L. F., et al. 1997, ApJ, 489, 744
Vaillancourt, J. E. 2006, PASP, 118, 1340
Vallee, J. P., & Bastien, P. 1995, A&A, 294, 831
van der Walt, S. J., Kristensen, L. E., Jørgensen, J. K., et al. 2021, A&A, 655, A86
Watson, C., Churchwell, E., Pankonin, V., & Bieging, J. H. 2002, ApJ, 577, 260
Zhang, Q., Qiu, K., Girart, J. M., et al. 2014, ApJ, 792, 116